Atmospheric River Life Cycle Responses to the Madden Julian Oscillation

Yang Zhou[1], Hyemi Kim[2], and Duane Waliser[3]

[1]Lawrence Berkeley National Laboratory
[2]Stony Brook University
[3]Jet Propulsion Laboratory

November 26, 2022

Abstract

We investigate how the Madden-Julian Oscillation (MJO), the dominant mode of tropical subseasonal variability, modulates the life cycle of cool-season North Pacific atmospheric rivers (ARs), low-level jets of intensive poleward moisture transport. When the MJO convection is over the Indian Ocean, more AR events originate over eastern Asia and fewer originate over the subtropical northern Pacific. The opposite changes in the number and location of AR events appear when the MJO convection is over the western Pacific. Dynamical processes involving anomalous MJO wind and seasonal mean moisture are found to be dominant factors that impact AR origins. The anomalous geopotential height pattern of the MJO can modulate AR propagation directions. The robustness of these MJO-AR life cycle connections is further supported by model simulations. The modulation of AR life cycles by the MJO may help to further advance our understanding of subseasonal predictability and future changes of ARs.

Atmospheric River Life Cycle Responses to the Madden Julian Oscillation

Yang Zhou[1*], Hyemi Kim[2], and Duane E. Waliser[3]

[1]Lawrence Berkeley National Laboratory, Berkeley, CA, 94720

[2]Stony Brook University, Stony Brook, NY, 11794

[3]Jet Propulsion Laboratory, California Institute of Technology, Pasadena, CA, 91109

*Corresponding author: Yang Zhou (yzhou2@lbl.gov)

Key Points:

- The Madden-Julian Oscillation significantly influences the number, lifetime, and propagation of North Pacific atmospheric rivers.
- More atmospheric rivers with longer lifetime occurs over the subtropical North Pacific when enhanced convection is over the western Pacific.
- Dynamical processes are the dominant factors in the modulation of atmospheric rivers by the Madden-Julian Oscillation.

Abstract

We investigate how the Madden-Julian Oscillation (MJO), the dominant mode of tropical subseasonal variability, modulates the life cycle of cool-season North Pacific atmospheric rivers (ARs), low-level jets of intensive poleward moisture transport. When the MJO convection is over the Indian Ocean, more AR events originate over eastern Asia and fewer originate over the subtropical northern Pacific. The opposite changes in the number and location of AR events appear when the MJO convection is over the western Pacific. Dynamical processes involving anomalous MJO wind and seasonal mean moisture are found to be dominant factors that impact AR origins. The anomalous geopotential height pattern of the MJO can modulate AR propagation directions. The robustness of these MJO-AR life cycle connections is further supported by model simulations. The modulation of AR life cycles by the MJO may help to further advance our understanding of subseasonal predictability and future changes of ARs.

Plain Language Summary

Atmospheric rivers (ARs) are strong moisture transport that conveys water vapor from the tropics to high latitudes, which are important water sources to coastal regions like the west coast of North America. Here we investigate the connections between the life cycle of ARs over the northern Pacific and the Madden-Julian Oscillation (MJO) which is one of the most dominant tropical variabilities. Results indicate that the MJO can affect the whole lifecycle of ARs including the origin, propagation, and termination. ARs are more active during certain MJO phases, which can be explained by the changes in wind and geopotential height that response to the MJO. Theses findings can help studies to better predict AR activity and understand how ARs will change in the future.

1. Introduction

In the past two decades, atmospheric rivers (ARs) have garnered continuous scientific interest and public attention due to their contributions to regional hydrological impacts including sources of freshwater supply, snow accumulation, floods, and precipitation extremes (Dettinger, 2013; Gorodetskaya et al., 2014; Guan et al., 2010, 2013; Kamae et al., 2017; Lavers et al., 2011; Nash et al., 2018; Neiman et al., 2013; Waliser & Guan, 2017). While ARs are closely associated with mid-latitude synoptic systems (J. W. Bao et al., 2006; Dacre et al., 2015; Z. Zhang et al., 2019), their activity is significantly modulated by low-frequency tropical variabilities like the Madden Julian Oscillation (MJO, Madden and Julian (1972)) (Guan & Waliser, 2015; Mundhenk et al., 2016; Payne & Magnusdottir, 2014), which has shown exceptional impacts on mid-latitude weather and climates (Ferranti et al., 1989; Stan et al., 2017; C. D. Zhang, 2013) such as storm tracks (Deng & Jiang, 2011; Zheng et al., 2018), blockings (Hamill & Kiladis, 2014; Henderson et al., 2016), and the Pacific-North America Pattern (Mori & Watanabe, 2008; Wang et al., 2020; W. Zhou et al., 2020). The landfalling ARs over North America and the associated California precipitation and snow accumulation are significantly intensified when the MJO convection is over the western Pacific (Guan et al., 2013; Guan et al., 2012; Payne & Magnusdottir, 2014). Given that the MJO is the dominant source of subseasonal predictability (Brunet et al., 2010; H. Kim et al., 2018; C. D. Zhang, 2013), the prediction of landfalling ARs can be extended to 3-5 weeks considering the MJO-AR connections (Baggett et al., 2017; DeFlorio et al., 2018; DeFlorio et al., 2019; Mundhenk et al., 2018).

An AR event generally originates in the ocean and terminates after landfall (Guan & Waliser, 2019; Xu et al., 2020; Y. Zhou et al., 2018). The life cycle of AR, which is the spatiotemporal evolution, can be modulated by atmospheric circulation (Guirguis et al., 2018; Y.

Zhou & Kim, 2019). Though, it remains elusive through what physical processes the MJO modulates the entire life cycle of AR from its origin to termination. Thus far, the MJO's impact on an AR life cycle has only been discussed for a single landfalling AR event that occurred in March 2005 (Ralph et al., 2011). A better understanding of MJO-AR life cycles relationship can further help to improve the prediction of AR events and associated hydrological impacts. The goal of this study is to explore the physical mechanisms associated with the changes in AR life cycles (origin, evolution, and termination) and their characteristics (number, lifetime, and intensity) affected by the MJO. The strong coupling between tropical moisture and convection is one of the key processes that explain the MJO dynamics (Adames & Kim, 2016; Bretherton et al., 2004; Holloway & Neelin, 2009; H. Kim et al., 2019) which distinguishes the MJO from other equatorial waves (Yasunaga & Mapes, 2012). Since large moisture anomalies are one of the necessary conditions for AR development, moisture changes associated with the MJO convection may play a key role in influencing AR life cycles. In addition, the MJO may modulate AR life cycles via the teleconnection pattern related to the MJO diabatic heating anomalies as they move eastward. These hypotheses are tested with long historical high-resolution reanalysis data and numerical model simulations.

2. Data and Methods

2.1. Reanalysis

To investigate ARs, we use vertically-integrated water vapor transport (IVT), which is calculated as

$$\mathrm{IVT} = -\frac{1}{g}\int_{1000\,hPa}^{300\,hPa} q\vec{V}\,dp, \quad (1)$$

where g is the gravitational acceleration (m s^{-2}), p is pressure (hPa), q is specific humidity (kg kg^{-1}), and $\vec{V}$ is horizontal wind vector (m s^{-1}). To calculate IVT, 20 vertical levels (1000-300 hPa) of 1.0° horizontal grid 6-hourly horizontal winds and specific humidity from ECMWF Interim Reanalysis (ERAI, Dee et al. (2011)) are used. We use 850 hPa 1.0° daily geopotential height (hereafter, Z850) from ERAI to analyze AR-related circulations. 1.0° daily vertically-integrated specific humidity is calculated as precipitable water (PW) to indicate the moisture associated with the MJO convection. The daily anomaly is calculated by subtracting the respective daily climatology. A 20-100-day Lanczos filtering is applied to daily anomalies to represent MJO-related signals. The period is from November to March when the MJO and North Pacific ARs are the most active (Guan & Waliser, 2015; Mundhenk et al., 2016; Stan et al., 2017) from 1979 to 2018. We use daily interpolated 20-100-day-filtered out-going longwave radiation (OLR) (Liebmann & Smith, 1996) to indicate the MJO convection.

2.2. The Madden-Julian Oscillation

We obtain the Real-time Multivariate MJO (RMM, Wheeler and Hendon (2004)) index to describe the MJO phase and amplitude. The RMM index consists of two principal components of a covariance matrix constructed by combined daily anomalies of OLR and zonal winds at 850 and 200 hPa in the tropics. The MJO is distinguished into eight phases using two RMM components. In this study, an MJO day is defined if the RMM amplitude ($\sqrt{\mathrm{RMM1}^2 + \mathrm{RMM2}^2}$) exceeds 1.0. We only select the MJO days that are concurrent with AR origins (about 39% of total MJO days) for composite analysis. To make the results more concise and to increase sample sizes, we reduce the eight MJO phases into four groups (phases 8-1, 2-3, 4-5, and 6-7) (Jeong et al., 2008; Li et al., 2016) and focus on the MJO phases 2-3 and 6-7 when the most significant changes in lifecycle frequency are shown (Supplemental S1). Phase 2-3 (phase 6-7) is defined as the MJO enhanced convection located over the Indian Ocean (western Pacific).

2.3 Life cycle of ARs

To identify the life cycle of AR events, we first detect AR object which is defined as an enclosed two-dimensional (latitude and longitude) instantaneous area of strong IVT that exceeds certain criteria of AR conditions (Fig. 1a). We follow the detection method developed by Guan and Waliser (2015) with minor modifications. The AR life cycle is tracked by connecting AR objects spatiotemporally from origin to termination (Y. Zhou et al., 2018). Example of a phase 6 MJO and AR life cycle during December 13-17, 2017 is shown in Fig. 1b. We categorize the AR events that originate between 0°N-60°N, 100°E-110°W (dash box in Fig. 1a) by MJO phases. Changes of AR activity is not sensitive to domain boundary. For each MJO phase, an AR event is selected based on whether the origin is concurrent with that MJO phase (e.g., Fig. 1b). Overall, approximately 63% of total AR events are selected.

The lifecycle frequency is calculated as the grid-point-accumulated number of AR objects (Fig. 1b) within one life cycle (Fig. 1c). Therefore, the lifecycle frequency is a density distribution that indicates the spatial occurrence of AR conditions (i.e. number of AR objects). We normalized the winter climatological mean of lifecycle frequency by dividing the total number of 6-hourly time steps during 39 winters (Fig. 2a). The composites of lifecycle frequency are constructed as follows: (i) for each MJO phase, select North Pacific AR events that *originate* concurrently with the MJO and calculate the lifecycle frequency; (ii) sum up the lifecycle frequency from selected AR events and subtract the winter climatological mean (Fig. 2a). Fig. 2b-c show the percentage changes in lifecycle frequency during phase 2-3 and 6-7 relative to the winter climatological mean.

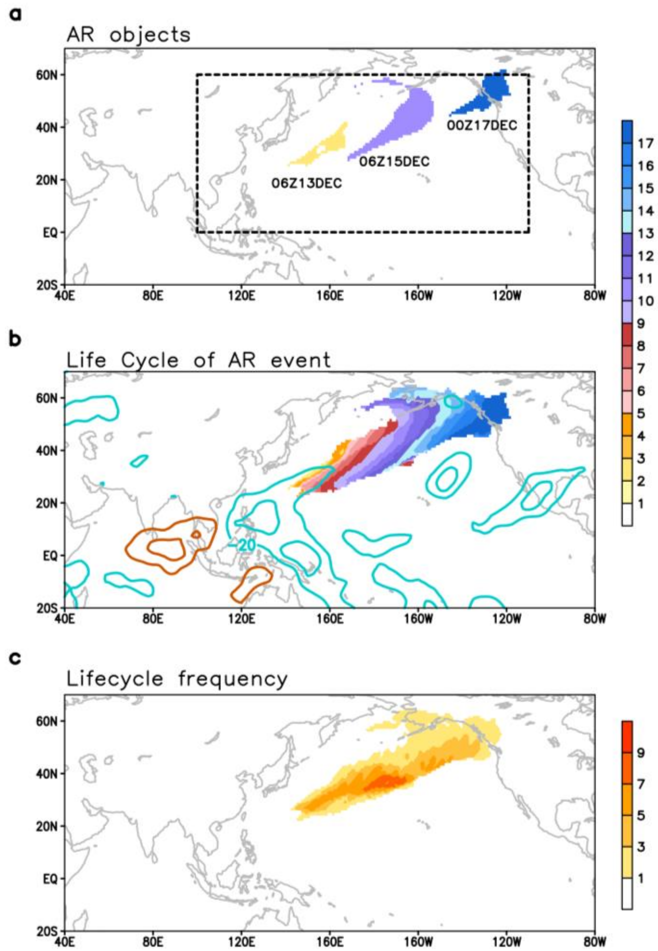

Figure 1. Example of **a** AR objects, **b** life cycle, and **c** lifecycle frequency (number of objects) of a landfalling AR event during December 13-17, 2017. Dash box (0°-60°N, 100°E-110 °W) in **a** shows the focused region for AR life cycles in this study. Shadings in **a-b** represent the binary masks of AR objects in 6-hourly time steps starting from the origin (December 13 00z). Orange/blue contours in **b** are 20-100-day-filtered OLR anomaly for positive/negative values (20 W m^{-2} interval, zero is omitted).

2.4 Moisture budget decomposition

We conduct moisture budget analysis on the anomalous moisture flux convergence (MFC). Similar to previous studies (H. Kim et al., 2017; Newman et al., 2012), we first decompose the total MFC field into climatological mean, and anomalies and nonlinear interaction between different time scales. Then, we only focus on the portion that is associated with the MJO (20-100-day filtered), which is represented by:

$$(\mathrm{MFC})' = (-\nabla \cdot \langle \overline{q} V' \rangle) + (-\nabla \cdot \langle q' \overline{V} \rangle) + (-\nabla \cdot \langle q' V' \rangle), (2)$$

where the angled bracket represents the vertical integration, the overhead bar denotes the seasonal mean, and the prime sign marks the 20-100-day-filtered daily anomalies. Therefore, the left-hand side can be interpreted as the total anomalous MFC associated with the MJO. The right-hand side represents the contribution from dynamic, thermodynamic, and nonlinear components, respectively.

2.5 ECMWF AMIP simulations

The robustness of the MJO-AR relationship is examined in ECMWF AMIP simulations (ECMWF-Hist) with 10 ensemble members (Davini et al., 2017). The model initial conditions are extracted from ERAI using the midnight values of the first 10 days starting from 1 January 1979, respectively. The sea surface temperature (SST) is obtained from the daily SST and sea ice concentration from Hadley Centre Sea Ice and SST dataset. The AMIP experiment extends from 1979-2008, but the output was only available from 1980-2000 (20 winters) at the time of our analysis. Therefore, there are total of 200 winters of simulations. The model's horizontal resolution is T255 (~80 km) and is bi-linearly interpolated to 1.0° grid to match with observations. The model's RMM index is obtained by projecting the model's OLR and 850 and 200 hPa zonal winds onto the observed eigenvectors from Wheeler and Hendon (2004). We pre-process the OLR and zonal winds by bi-linearly interpolating to 2.5° grid, removing the mean of the most recent 120 days of model analysis, and dividing the observed normalization factors (details in Gottschalck et al. (2010)). The AR object detection in ECMWF-Hist is the same as ERAI. We treat each ensemble member equally and the ensemble mean is the average of selected AR life cycles from 10 ensembles. We calculate the signal-to-noise ratio by dividing the signal which is the external forcing (ensemble mean of anomalous AR frequency) by the noise which is the atmospheric internal variability (one standard deviation of anomalous AR frequency across 10 ensemble members).

3. MJO's impact on AR life cycles

North Pacific AR activity peaks during boreal winter (Guan & Waliser, 2015; Mundhenk et al., 2016). Climatologically, the maximum lifecycle frequency emerges between 25°N-60°N over the central North Pacific, indicating that more than 10% of the time over the region is affected by ARs (Fig. 2a). During phase 2-3 (Fig. 2b), a zonally oriented anomalous high pressure prevails over the North Pacific and induces anomalous anticyclonic flow. Over eastern Asia, including the east coast of China, South Korea, and Japan, AR lifecycle frequency is increased by 10-20% corresponding to a positive anomaly in poleward IVT to the west of the anomalous high. Over the subtropical North Pacific, lifecycle frequency is significantly suppressed by 50-60% which is associated with the anticyclonic flow. Changes in lifecycle frequency are linked to changes in the number of AR events, lifetime (i.e. how long an AR life cycle lasts), and life cycle intensity (the mean IVT magnitude during the life cycle) (Y. Zhou et al., 2018). Over the North Pacific, all three factors (i.e. number, lifetime, and lifecycle intensity) consistently decrease during phase 2-3 (Fig. 2d). Overall, during MJO phase 2-3, the number of North Pacific AR events decreases by 6.7% with significantly shortened lifetime and weakened intensity compared to climatology.

Changes in lifecycle frequency during phase 6-7 (Fig. 2c) shows nearly opposite features from phase 2-3. Lifecycle frequency is reduced by about 30% over the northwestern Pacific which is associated with the equatorward and westward IVT anomaly at the west of the prevailing anomalous low over the North Pacific. The anomalous low and cyclonic flow significantly prompt AR activity, by an increase of 30-60% over the central Pacific and 20-30% over northwestern North America. The AR activity near Hawaii, known as Pineapple Express, is more frequent during MJO phase 6-7 which potentially leads to more AR landfalls over the west coast of North America (Guan et al., 2012; Payne & Magnusdottir, 2014; Spry et al., 2014). The number of AR events increases by nearly 5% during phase 6-7 with significantly longer lifetime and stronger intensity (Fig. 2d).

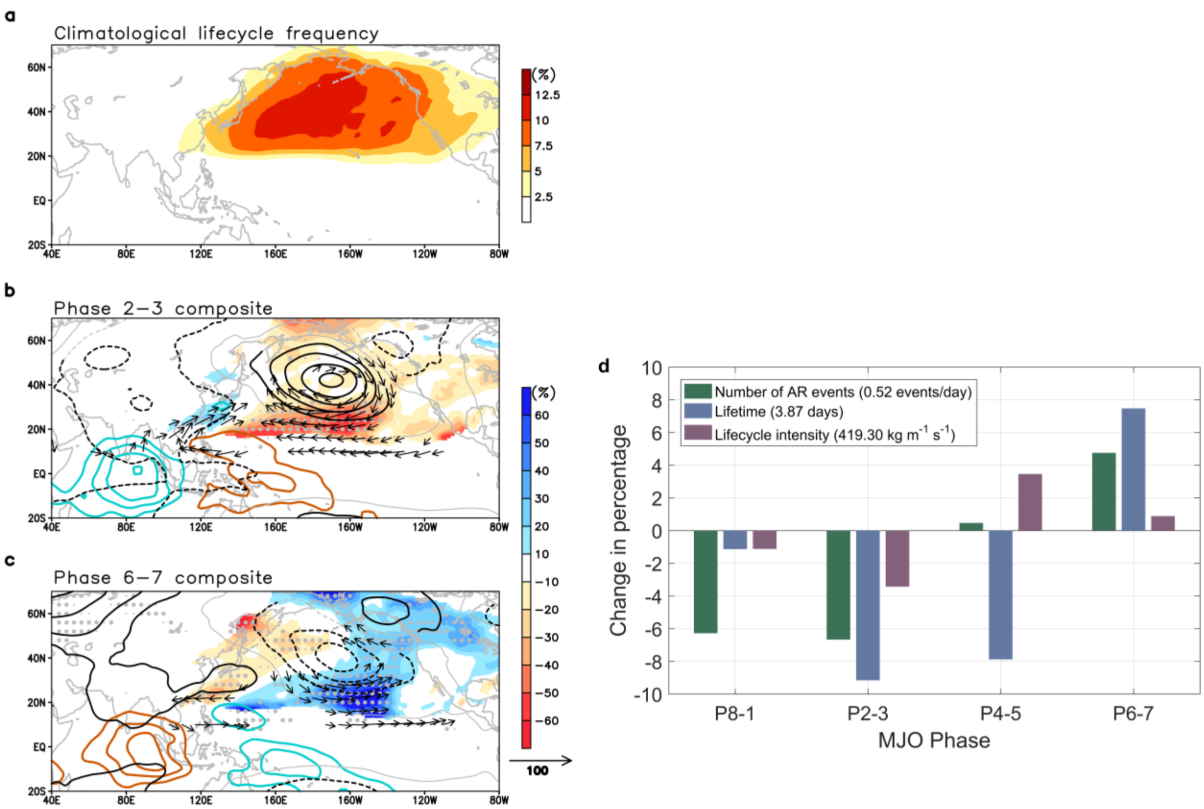

Figure 2 a Winter climatological lifecycle frequency (percent of time steps) with North Pacific AR events (originated in the black dash box in Figure **1a**). **b-c** Percentage changes in lifecycle frequency with respect to **a** (shading), Z850 anomaly (solid/dash contours represent positive/negative values, 5m interval), IVT anomaly (only showing values to the north of 10°N and over 15 kg m^{-1} s^{-1}), and OLR anomaly (orange/blue contours represent positive/negative values, 5 W/m^2 interval, zero line is omitted) for the MJO **b** phase 2-3 and **c** phase 6-7. Z850 and IVT anomalies are 10-day averaged starting from AR origins. The OLR anomaly is concurrent with AR origins. The large (small) grey dots mark AR frequency anomalies that pass the 95% (90%) confidence level of one-sample t-test. Black contours and vectors represent values that exceed the 95% confidence level of one-sample t-test. **d** Percentage changes in the number of

AR events, lifetime, and lifecycle intensity over the North Pacific. Numbers in the legend denote the climatological mean.

4. Physical mechanism behind the MJO-AR life cycle relationship

By examining the day-by-day evolution of AR life cycles, we found that the temporal propagation of ARs roughly aligns with the geopotential height anomalies. During the MJO phase 2-3, increased frequency of AR origins occurs over eastern Asia (Fig. 3a and Supplemental S2a). The increased frequency extends northward along the northwest flank of the anomalous high and gradually dissipates about four days after AR origins (Supplemental S2c), likely due to the overall less moisture content in the higher latitudes that expedites the termination of AR events (Trenberth, 1998). Meanwhile, the decreased frequency associated with the anticyclonic flow persists over the subtropical Pacific until six days after AR origins (Supplemental S2d). In contrast, during phase 6-7, increased (decreased) frequency of AR origins occurs over the subtropical northwestern Pacific (eastern Asia) (Fig. 3b and Supplemental S2f). After AR origins, the increased frequency amplifies as it extends eastward and northward for six days, accompanied by the anomalous low and cyclonic flow (Supplemental S2f-i).

The results discussed above show that the MJO influences the entire AR life cycle including the origins. Through what physical processes does the MJO influence the origin of ARs? Studies have elucidated that the MJO associated tropical heating induces the Matsuno-Gill response (M. Bao & Hartmann, 2014; Gill, 1980; Matsuno, 1966) and the enhanced tropical convection is strongly coupled to moisture (Bretherton et al., 2004). During MJO phase 2-3 (Fig. 3a), higher precipitable water is observed in the Indo-Pacific and East Asia. Two anticyclonic anomalies arise near 135°E on each side of the equator, which is to the west of the suppressed convection over the western Pacific, a typical Matsuno-Gill type response. The associated poleward anomalous wind near 30°N, 120°E advects the positive moisture anomaly from the Indian Ocean. The positive IVT anomaly supports the increase of AR origins over eastern Asia. Meanwhile, decreased frequency of AR origins near 160°E is associated with the southwestward IVT anomaly related to the decreased moisture and southward wind anomalies. Conversely, during MJO phase 6-7 (Fig. 3b), Indo-Pacific and eastern Asia are dryer overall and two cyclonic flow anomalies straddle the equator over the western Pacific. Decreased frequency of AR origins over eastern Asia is attributed to the decreased moisture and southwestward wind anomaly. The increased moisture and cyclonic flow anomalies facilitate the increased AR origin frequency near 150°E. Besides, for both phases 2-3 and 6-7, changes in origin frequency over the subtropical central Pacific are aligned with the southern flank of geopotential height anomaly and facilitated by the corresponding anomalous IVT (Fig. 3a-b).

To better understand the relative contributions from dynamic (wind), thermodynamic (moisture), and nonlinear processes, we decompose the anomalous moisture flux convergence that corresponds to areas of increased frequency of AR origins (yellow boxes in Fig. 3a-b). Results indicate that the dynamical process related to the patterns of seasonal mean moisture and anomalous MJO wind contributes the most to changes in total moisture flux convergence in MJO phases 2-3 and 6-7 (Fig. 3c-d). The thermodynamic process, which is associated with seasonal mean wind and the MJO moisture anomaly, contributes negatively to the total changes: although the moisture anomaly becomes positive as the MJO propagates, a positive meridional gradient in seasonal mean meridional wind leads to a decrease in local moisture flux convergence. The nonlinear component associated with the MJO moisture and wind anomalies is negligible for both phases. Moreover, the amplitude difference in total moisture flux convergence anomaly between MJO phases 2-3 and 6-7 is primarily due to the meridional gradient of mean moisture

(Fig. 4): over the subtropical northwestern Pacific (where AR origin is enhanced during phase 2-3), the meridional distribution of mean moisture is steeper than that over the tropics (where AR origin is enhanced during phase 6-7).

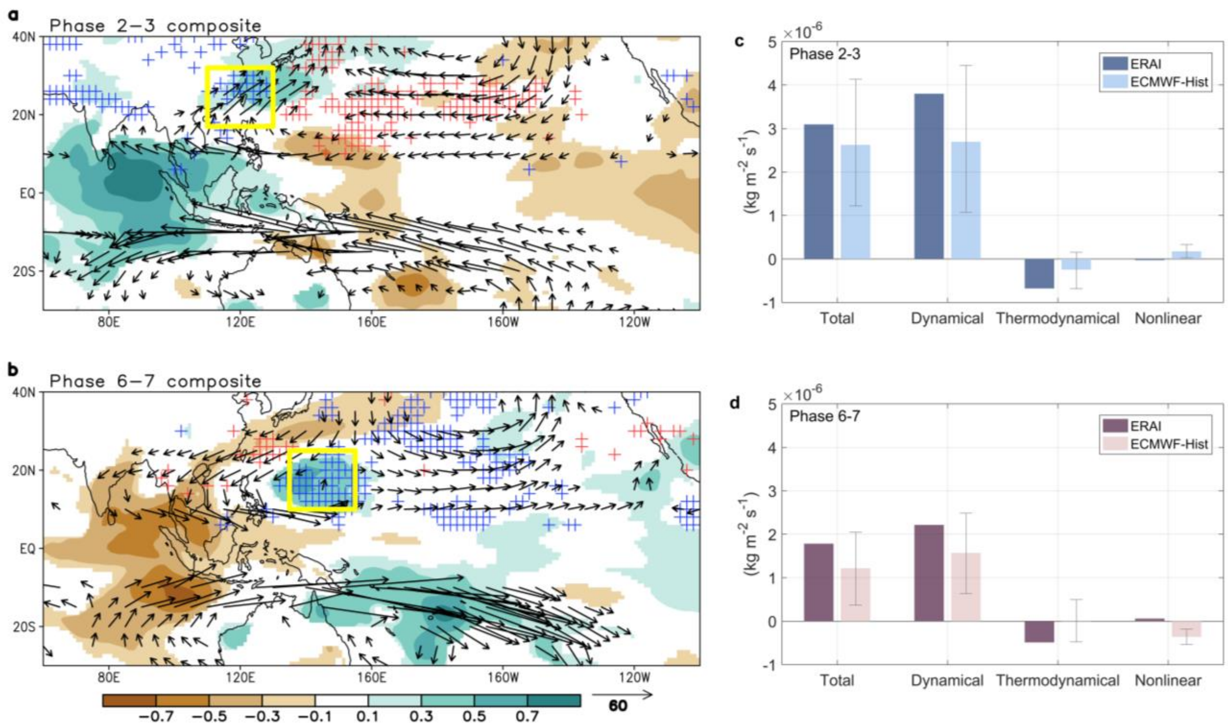

Figure 3. 20-100-day-filtered precipitable water anomaly (shading, kg m^{-2}) and IVT anomaly (vectors, only showing values outside of 10°S-10°N and over 10 kg m^{-1} s^{-1}), and AR origin frequency anomaly (blue/red cross markers represent positive/negative values that pass the 90% confidence level of one-sample t-test) for the MJO **a** phase 2-3 and **b** phase 6-7. Vectors and shadings represent values that pass the 95% confidence level of one-sample t-test. **c-d** Moisture budget terms for the MJO **c** phase 2-3 and **d** phase 6-7 averaged within the yellow box (17°N-32°N, 110°E-130°E in **a** and 10°N-25°N, 135°E-155°E in **b**) using ERA-I and ECMWF-Hist. The bars in **c-d** show the ensemble means of ECMWF-Hist and the error bars show the one standard deviation of 10 ensemble members.

The extent to which the observed MJO-AR life cycle relationship is affected by the atmospheric internal variability is unclear. To expand sample sizes and to evaluate the robustness of the observed connection, the representation of MJO-AR lifecycle is examined in ECMWF AMIP simulations, which have shown improvement in simulating the MJO (Davini et al., 2017).

Overall, the simulated changes in lifecycle frequency are roughly consistent with the observation, albeit with weaker amplitude and regional biases (Supplemental S3a-b). The model simulates the observed physical processes (Fig. 3c-d), which indicates the dominant role of the MJO-related wind in the MJO-AR life cycle connection. With the presence of internal variability (noise), changes in simulated AR activity over the North Pacific are largely controlled by the MJO (signal) (Supplemental S3c-d).

5. Summary and implications

We explore the physical processes of the MJO-AR life cycle relationship over the North Pacific by tracking the life cycle of ARs from their origin to termination. Fig. 4 summarizes the key results. Changes in AR life cycle are the most significant during MJO phase 2-3 and 6-7 when a dipole of enhanced and suppressed convections locates over the Indian Ocean and the western Pacific. During MJO phase 2-3, increased (decreased) frequency of AR origins occurs over eastern Asia (the northwestern Pacific), which is associated with the anticyclonic flows over the subtropical western Pacific in response to the MJO heating. The propagation of ARs is influenced by the persistent anomalous high as the MJO mid-latitude teleconnection, with decreased (increased) AR activity over the subtropical central Pacific (northwestern Pacific). Opposite features to those described above emerge during MJO phase 6-7. The anomalous low prevails over the northern Pacific and guides ARs to propagate towards northeastward. AR activity is decreased at the northwest of the anomalous low. Responses in AR life cycle are influenced most strongly by the MJO wind anomaly pattern and the mean moisture. Model simulations further support the robustness of the relation of the MJO and AR life cycles.

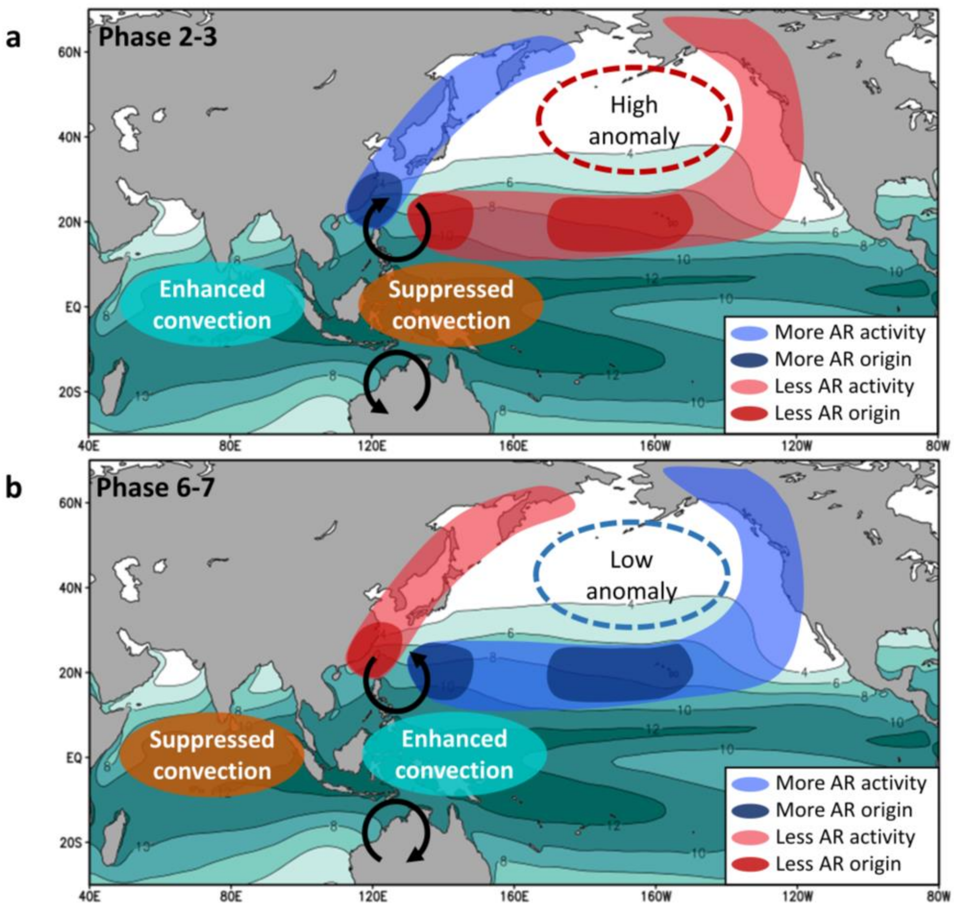

Figure 4. Schematic diagrams of the MJO's impact on AR life cycles during the MJO **a** phase 2-3 and **b** phase 6-7. Background shading is 850 hPa specific humidity climatology (g/kg). Curved black arrows mark the anomalous 850 hPa wind as Matsuno-Gill response.

Since ARs are often synonymous with severe weather events, improving subseasonal prediction of ARs is of great importance to facilitate emergency preparedness and to mitigate socio-economic losses (Dominguez et al., 2018; Ralph et al., 2019). While previous studies mainly focus on the prediction of landfalling AR frequency related to the MJO (Baggett et al., 2017; DeFlorio et al., 2018; DeFlorio et al., 2019; Mundhenk et al., 2018), the analyzed connection between the MJO and AR life cycle may potentially help to improve the subseasonal prediction of ARs utilizing the correspondence between AR origins and terminations (which are often caused by precipitation at landfalls). For instance, with a given MJO phase or its forecasted state, one could possibly forecast the life cycle of an AR event including its likely propagation track and termination location, and further its hydrological impacts.

Finally, questions have been raised about how ARs will change in the future climate. AR occurrence is projected to increase (Dettinger, 2011; Lavers et al., 2013; Warner et al., 2015) with wider geometric shapes, stronger intensities, and a northward shift of landfall locations (Espinoza et al., 2018; Radic et al., 2015; Shields & Kiehl, 2016). The MJO is projected to have deeper and larger convection and to travel further eastward with increasing phase speed (Adames et al., 2017; Chang et al., 2015; Maloney et al., 2019). The current study provides a scientific basis and useful tool to examine the MJO-AR connection in the context of future climate.

Data Availability Statement

ERA-Interim data were obtained freely from http://apps.ecmwf.int/datasets/data/interim_full_daily. The OLR is provided by the NOAA/OAR/ESRL PSD, Boulder, Colorado, USA, from their Web site at https://psl.noaa.gov/data/gridded/data.interp_OLR.html. The RMM index is obtained from the Bureau of Meteorology from Australian Government (http://www.bom.gov.au/climate/mjo/graphics/rmm.74toRealtime.txt). The ECMWF AMIP simulation is provided by Dr. Aneesh Subramanian which can be downloaded through a dedicated THREDDS Web Server hosted by CINECA (https://sphinx.hpc.cineca.it/thredds/catalog/SPHINX/catalog.html).

Acknowledgement

YZ was supported by NSF Grant AGS-1652289 and the U.S. Department of Energy, Office of Science, Office of Biological and Environmental Research, Climate and Environmental Sciences Division, Regional & Global Climate Modeling Program, under Award DE-AC02-05CH11231. HK was supported by NSF Grant AGS-1652289 and the KMA R&D Program Grant KMI2018-03110. DEW's contribution to this study was carried out on behalf of the Jet Propulsion Laboratory, California Institute of Technology, under a contract with the National Aeronautics and Space Administration.

Reference

Adames, A. F., & Kim, D. (2016). The MJO as a Dispersive, Convectively Coupled Moisture Wave: Theory and Observations. *Journal of the Atmospheric Sciences, 73*(3), 913-941. doi:10.1175/Jas-D-15-0170.1

Adames, A. F., Kim, D., Sobel, A. H., Del Genio, A., & Wu, J. (2017). Changes in the structure and propagation of the MJO with increasing CO2. *J Adv Model Earth Syst, 9*(2), 1251-1268. doi:10.1002/2017MS000913

Baggett, C. F., Barnes, E. A., Maloney, E. D., & Mundhenk, B. D. (2017). Advancing atmospheric river forecasts into subseasonal-to-seasonal time scales. *Geophysical Research Letters, 44*(14), 7528-7536. doi:10.1002/2017gl074434

Bao, J. W., Michelson, S. A., Neiman, P. J., Ralph, F. M., & Wilczak, J. M. (2006). Interpretation of enhanced integrated water vapor bands associated with extratropical cyclones: Their formation and connection to tropical moisture. *Monthly Weather Review, 134*(4), 1063-1080. doi:Doi 10.1175/Mwr3123.1

Bao, M., & Hartmann, D. L. (2014). The response to MJO-like forcing in a nonlinear shallow-water model. *Geophysical Research Letters, 41*(4), 1322-1328. doi:10.1002/2013gl057683

Bretherton, C. S., Peters, M. E., & Back, L. E. (2004). Relationships between water vapor path and precipitation over the tropical oceans. *Journal of Climate, 17*(7), 1517-1528. doi:Doi 10.1175/1520-0442(2004)017<1517:Rbwvpa>2.0.Co;2

Brunet, G., Shapiro, M., Hoskins, B., Moncrieff, M., Dole, R., Kiladis, G. N., . . . Shukla, J. (2010). Collaboration of the Weather and Climate Communities to Advance Subseasonal-to-Seasonal Prediction. *Bulletin of the American Meteorological Society, 91*(10), 1397-1406. doi:10.1175/2010bams3013.1

Chang, C. W. J. N., Tseng, W. L., Hsu, H. H., Keenlyside, N., & Tsuang, B. J. (2015). The Madden-Julian Oscillation in a warmer world. *Geophysical Research Letters, 42*(14), 6034-6042. doi:10.1002/2015gl065095

Dacre, H. F., Clark, P. A., Martinez-Alvarado, O., Stringer, M. A., & Lavers, D. A. (2015). How Do Atmospheric Rivers Form? *Bulletin of the American Meteorological Society, 96*(8), 1243-1255. doi:10.1175/bams-d-14-00031.1

Davini, P., von Hardenberg, J., Corti, S., Christensen, H. M., Juricke, S., Subramanian, A., . . . Palmer, T. N. (2017). Climate SPHINX: evaluating the impact of resolution and stochastic physics parameterisations in the EC-Earth global climate model. *Geoscientific Model Development, 10*(3), 1383-1402. doi:10.5194/gmd-10-1383-2017

Dee, D. P., Uppala, S. M., Simmons, A. J., Berrisford, P., Poli, P., Kobayashi, S., . . . Vitart, F. (2011). The ERA-Interim reanalysis: configuration and performance of the data assimilation system. *Quarterly Journal of the Royal Meteorological Society, 137*(656), 553-597. doi:10.1002/qj.828

DeFlorio, M. J., Waliser, D. E., Guan, B., Ralph, F. M., & Vitart, F. (2018). Global evaluation of atmospheric river subseasonal prediction skill. *Climate Dynamics, 52*(5-6), 3039-3060. doi:10.1007/s00382-018-4309-x

DeFlorio, M. J., Waliser, D. E., Ralph, F. M., Guan, B., Goodman, A., Gibson, P. B., . . . Kumar, A. (2019). Experimental Subseasonal-to-Seasonal (S2S) Forecasting of Atmospheric Rivers Over the Western United States. *Journal of Geophysical Research: Atmospheres, 124*(21), 11242-11265. doi:10.1029/2019jd031200

Deng, Y., & Jiang, T. Y. (2011). Intraseasonal Modulation of the North Pacific Storm Track by Tropical Convection in Boreal Winter. *Journal of Climate, 24*(4), 1122-1137. doi:10.1175/2010jcli3676.1

Dettinger, M. D. (2011). Climate Change, Atmospheric Rivers, and Floods in California - A Multimodel Analysis of Storm Frequency and Magnitude Changes. *Journal of the American Water Resources Association, 47*(3), 514-523. doi:10.1111/j.1752-1688.2011.00546.x

Dettinger, M. D. (2013). Atmospheric Rivers as Drought Busters on the US West Coast. *Journal of Hydrometeorology, 14*(6), 1721-1732. doi:10.1175/Jhm-D-13-02.1

Dominguez, F., Dall'erba, S., Huang, S., Avelino, A., Mehran, A., Hu, H., . . . Lettenmaier, D. (2018). Tracking an atmospheric river in a warmer climate: from water vapor to economic impacts. *Earth Syst. Dynam., 9*(1), 249-266. doi:10.5194/esd-9-249-2018

Espinoza, V., Waliser, D. E., Guan, B., Lavers, D. A., & Ralph, F. M. (2018). Global Analysis of Climate Change Projection Effects on Atmospheric Rivers. *Geophysical Research Letters, 45*(9), 4299-4308. doi:10.1029/2017gl076968

Ferranti, L., Palmer, T. N., Molteni, F., & Klinker, E. (1989). Tropical-Extratropical Interaction Associated with the 30–60 Day Oscillation and Its Impact on Medium and Extended Range Prediction. *Journal of the Atmospheric Sciences, 47*(18), 2177-2199. doi:10.1175/1520-0469(1990)047<2177:Teiawt>2.0.Co;2

Gill, A. E. (1980). Some simple solutions for heat-induced tropical circulation. *Quarterly Journal of the Royal Meteorological Society, 106*(449), 447-462. doi:10.1002/qj.49710644905

Gorodetskaya, I. V., Tsukernik, M., Claes, K., Ralph, M. F., Neff, W. D., & Van Lipzig, N. P. M. (2014). The role of atmospheric rivers in anomalous snow accumulation in East Antarctica. *Geophysical Research Letters, 41*(17), 6199-6206. doi:10.1002/2014gl060881

Gottschalck, J., Wheeler, M., Weickmann, K., Vitart, F., Savage, N., Lin, H., . . . Higgins, W. (2010). A Framework for Assessing Operational Madden–Julian Oscillation Forecasts. *Bulletin of the American Meteorological Society, 91*(9), 1247-1258. doi:10.1175/2010bams2816.1

Guan, B., Molotch, N. P., Waliser, D. E., Fetzer, E. J., & Neiman, P. J. (2010). Extreme snowfall events linked to atmospheric rivers and surface air temperature via satellite measurements. *Geophysical Research Letters, 37*. doi:Artn L2040110.1029/2010gl044696

Guan, B., Molotch, N. P., Waliser, D. E., Fetzer, E. J., & Neiman, P. J. (2013). The 2010/2011 snow season in California's Sierra Nevada: Role of atmospheric rivers and modes of large-scale variability. *Water Resources Research, 49*(10), 6731-6743. doi:10.1002/wrcr.20537

Guan, B., & Waliser, D. E. (2015). Detection of atmospheric rivers: Evaluation and application of an algorithm for global studies. *Journal of Geophysical Research-Atmospheres, 120*(24), 12514-12535. doi:10.1002/2015jd024257

Guan, B., & Waliser, D. E. (2019). Tracking Atmospheric Rivers Globally: Spatial Distributions and Temporal Evolution of Life Cycle Characteristics. *Journal of Geophysical Research: Atmospheres, 124*(23), 12523-12552. doi:10.1029/2019jd031205

Guan, B., Waliser, D. E., Molotch, N. P., Fetzer, E. J., & Neiman, P. J. (2012). Does the Madden–Julian Oscillation Influence Wintertime Atmospheric Rivers and Snowpack in the Sierra Nevada? *Monthly Weather Review, 140*(2), 325-342. doi:10.1175/mwr-d-11-00087.1

Guirguis, K., Gershunov, A., Shulgina, T., Clemesha, R. E. S., & Ralph, F. M. (2018). Atmospheric rivers impacting Northern California and their modulation by a variable climate. *Climate Dynamics, 52*(11), 6569-6583. doi:10.1007/s00382-018-4532-5

Hamill, T. M., & Kiladis, G. N. (2014). Skill of the MJO and Northern Hemisphere Blocking in GEFS Medium-Range Reforecasts. *Monthly Weather Review, 142*(2), 868-885. doi:10.1175/mwr-d-13-00199.1

Henderson, S. A., Maloney, E. D., & Barnes, E. A. (2016). The Influence of the Madden-Julian Oscillation on Northern Hemisphere Winter Blocking. *Journal of Climate, 29*(12), 4597-4616. doi:10.1175/Jcli-D-15-0502.1

Holloway, C. E., & Neelin, J. D. (2009). Moisture Vertical Structure, Column Water Vapor, and Tropical Deep Convection. *Journal of the Atmospheric Sciences, 66*(6), 1665-1683. doi:10.1175/2008jas2806.1

Jeong, J., Kim, B., Ho, C., & Noh, Y. (2008). Systematic Variation in Wintertime Precipitation in East Asia by MJO-Induced Extratropical Vertical Motion. *Journal of Climate, 21*(4), 788-801. doi:10.1175/2007jcli1801.1

Kamae, Y., Mei, W., Xie, S.-P., Naoi, M., & Ueda, H. (2017). Atmospheric Rivers over the Northwestern Pacific: Climatology and Interannual Variability. *Journal of Climate, 30*(15), 5605-5619. doi:10.1175/jcli-d-16-0875.1

Kim, H., Janiga, M. A., & Pegion, K. (2019). MJO Propagation Processes and Mean Biases in the SubX and S2S Reforecasts. *Journal of Geophysical Research: Atmospheres, 124*(16), 9314-9331. doi:10.1029/2019jd031139

Kim, H., Vitart, F., & Waliser, D. E. (2018). Prediction of the Madden–Julian Oscillation: A Review. *Journal of Climate, 31*(23), 9425-9443. doi:10.1175/jcli-d-18-0210.1

Kim, H., Zhou, Y., & Alexander, M. A. (2017). Changes in atmospheric rivers and moisture transport over the Northeast Pacific and western North America in response to ENSO diversity. *Climate Dynamics*, 1-14. doi:10.1007/s00382-017-3598-9

Lavers, D. A., Allan, R. P., Villarini, G., Lloyd-Hughes, B., Brayshaw, D. J., & Wade, A. J. (2013). Future changes in atmospheric rivers and their implications for winter flooding in Britain. *Environmental Research Letters, 8*(3). doi:Artn 03401010.1088/1748-9326/8/3/034010

Lavers, D. A., Allan, R. P., Wood, E. F., Villarini, G., Brayshaw, D. J., & Wade, A. J. (2011). Winter floods in Britain are connected to atmospheric rivers. *Geophysical Research Letters, 38*(23), L23803. doi:Artn L2380310.1029/2011gl049783

Li, W., Guo, W., Hsu, P., & Xue, Y. (2016). Influence of the Madden–Julian oscillation on Tibetan Plateau snow cover at the intraseasonal time-scale. *Scientific Reports, 6*(1), 30456. doi:10.1038/srep30456

Liebmann, B., & Smith, C. A. (1996). Description of a complete (interpolated) outgoing longwave radiation dataset. *Bulletin of the American Meteorological Society, 77*(6), 1275-1277. Retrieved from <Go to ISI>://WOS:A1996VC04300013

Madden, R., & Julian, P. (1972). Further Evidence of Global-Scale, 5-Day Pressure Waves. *Journal of the Atmospheric Sciences, 29*(8), 1464-&. doi:Doi 10.1175/1520-0469(1972)029<1464:Feogsd>2.0.Co;2

Maloney, E. D., Adames, A. F., & Bui, H. X. (2019). Madden-Julian oscillation changes under anthropogenic warming. *Nature Climate Change, 9*(1), 26-33. doi:10.1038/s41558-018-0331-6

Matsuno, T. (1966). Quasi-Geostrophic Motions in the Equatorial Area. *Journal of the Meteorological Society of Japan. Ser. II, 44*(1), 25-43. doi:10.2151/jmsj1965.44.1_25

Mori, M., & Watanabe, M. (2008). Growth and triggering mechanisms of the PNA: A MJO-PNA coherence. *Journal of the Meteorological Society of Japan, 86*(1), 213-236. doi:DOI 10.2151/jmsj.86.213

Mundhenk, B. D., Barnes, E. A., & Maloney, E. D. (2016). All-Season Climatology and Variability of Atmospheric River Frequencies over the North Pacific. *Journal of Climate, 29*(13), 4885-4903. doi:10.1175/Jcli-D-15-0655.1

Mundhenk, B. D., Barnes, E. A., Maloney, E. D., & Baggett, C. F. (2018). Skillful empirical subseasonal prediction of landfalling atmospheric river activity using the Madden–Julian oscillation and quasi-biennial oscillation. *npj Climate and Atmospheric Science, 1*(1), 20177. doi:10.1038/s41612-017-0008-2

Nash, D., Waliser, D., Guan, B., Ye, H., & Ralph, F. M. (2018). The Role of Atmospheric Rivers in Extratropical and Polar Hydroclimate. *Journal of Geophysical Research: Atmospheres, 123*(13), 6804-6821. doi:10.1029/2017jd028130

Neiman, P. J., Ralph, F. M., Moore, B. J., Hughes, M., Mahoney, K. M., Cordeira, J. M., & Dettinger, M. D. (2013). The Landfall and Inland Penetration of a Flood-Producing Atmospheric River in Arizona. Part I: Observed Synoptic-Scale, Orographic, and Hydrometeorological Characteristics. *Journal of Hydrometeorology, 14*(2), 460-484. doi:10.1175/Jhm-D-12-0101.1

Newman, M., Kiladis, G. N., Weickmann, K. M., Ralph, F. M., & Sardeshmukh, P. D. (2012). Relative Contributions of Synoptic and Low-Frequency Eddies to Time-Mean Atmospheric Moisture Transport, Including the Role of Atmospheric Rivers. *Journal of Climate, 25*(21), 7341-7361. doi:10.1175/Jcli-D-11-00665.1

Payne, A. E., & Magnusdottir, G. (2014). Dynamics of Landfalling Atmospheric Rivers over the North Pacific in 30 Years of MERRA Reanalysis. *Journal of Climate, 27*(18), 7133-7150. doi:10.1175/Jcli-D-14-00034.1

Radic, V., Cannon, A. J., Menounos, B., & Gi, N. (2015). Future changes in autumn atmospheric river events in British Columbia, Canada, as projected by CMIP5 global climate models. *Journal of Geophysical Research-Atmospheres, 120*(18), 9279-9302. doi:10.1002/2015jd023279

Ralph, F. M., Neiman, P. J., Kiladis, G. N., Weickmann, K., & Reynolds, D. W. (2011). A Multiscale Observational Case Study of a Pacific Atmospheric River Exhibiting Tropical-Extratropical Connections and a Mesoscale Frontal Wave. *Monthly Weather Review, 139*(4), 1169-1189. doi:10.1175/2010mwr3596.1

Ralph, F. M., Rutz, J. J., Cordeira, J. M., Dettinger, M., Anderson, M., Reynolds, D., . . . Smallcomb, C. (2019). A Scale to Characterize the Strength and Impacts of Atmospheric Rivers. *Bulletin of the American Meteorological Society, 100*(2), 269-290. doi:10.1175/Bams-D-18-0023.1

Shields, C. A., & Kiehl, J. T. (2016). Atmospheric river landfall-latitude changes in future climate simulations. *Geophysical Research Letters, 43*(16), 8775-8782. doi:10.1002/2016gl070470

Spry, C. M., Kohfeld, K. E., Allen, D. M., Dunkley, D. M., & Lertzman, K. P. (2014). Characterizing Pineapple Express storms in the Lower Mainland of British Columbia, Canada. *Canadian Water Resources Journal / Revue canadienne des ressources hydriques, 39*(3), 302-323. doi:10.1080/07011784.2014.942574

Stan, C., Straus, D. M., Frederiksen, J. S., Lin, H., Maloney, E. D., & Schumacher, C. (2017). Review of Tropical-Extratropical Teleconnections on Intraseasonal Time Scales. *Reviews of Geophysics, 55*(4), 902-937. doi:10.1002/2016rg000538

Trenberth, K. E. (1998). Atmospheric Moisture Residence Times and Cycling: Implications for Rainfall Rates and Climate Change. *Climatic Change, 39*(4), 667-694. doi:10.1023/A:1005319109110

Waliser, D. E., & Guan, B. (2017). Extreme winds and precipitation during landfall of atmospheric rivers. *Nature Geoscience, 10*(3), 179-U183. doi:10.1038/Ngeo2894

Wang, J., Kim, H., Kim, D., Henderson, S. A., Stan, C., & Maloney, E. D. (2020). MJO Teleconnections over the PNA Region in Climate Models. Part I: Performance- and Process-Based Skill Metrics. *Journal of Climate, 33*(3), 1051-1067. doi:10.1175/jcli-d-19-0253.1

Warner, M. D., Mass, C. F., & Salathe, E. P. (2015). Changes in Winter Atmospheric Rivers along the North American West Coast in CMIP5 Climate Models. *Journal of Hydrometeorology, 16*(1), 118-128. doi:10.1175/Jhm-D-14-0080.1

Wheeler, M. C., & Hendon, H. H. (2004). An all-season real-time multivariate MJO index: Development of an index for monitoring and prediction. *Monthly Weather Review, 132*(8), 1917-1932. doi:Doi 10.1175/1520-0493(2004)132<1917:Aarmmi>2.0.Co;2

Xu, G., Ma, X., Chang, P., & Wang, L. (2020). A Comparison of Northern Hemisphere Atmospheric Rivers Detected by a New Image-Processing Based Method and Magnitude-Thresholding Based Methods. *Atmosphere, 11*(6), 628. Retrieved from https://www.mdpi.com/2073-4433/11/6/628

Yasunaga, K., & Mapes, B. (2012). Differences between More Divergent and More Rotational Types of Convectively Coupled Equatorial Waves. Part I: Space–Time Spectral Analyses. *Journal of the Atmospheric Sciences, 69*(1), 3-16. doi:10.1175/jas-d-11-033.1

Zhang, C. D. (2013). Madden–Julian Oscillation: Bridging Weather and Climate. *Bulletin of the American Meteorological Society, 94*(12), 1849-1870. doi:10.1175/bams-d-12-00026.1

Zhang, Z., Ralph, F. M., & Zheng, M. (2019). The Relationship Between Extratropical Cyclone Strength and Atmospheric River Intensity and Position. *Geophysical Research Letters, 46*(3), 1814-1823. doi:10.1029/2018gl079071

Zheng, C., Chang, E. K. M., Kim, H., Zhang, M., & Wang, W. (2018). Impacts of the Madden–Julian Oscillation on Storm-Track Activity, Surface Air Temperature, and Precipitation over North America. *Journal of Climate, 31*(15), 6113-6134. doi:10.1175/jcli-d-17-0534.1

Zhou, W., Yang, D., Xie, S., & Ma, J. (2020). Amplified Madden–Julian oscillation impacts in the Pacific–North America region. *Nature Climate Change, 10*(7), 654-660. doi:10.1038/s41558-020-0814-0

Zhou, Y., & Kim, H. (2019). Impact of Distinct Origin Locations on the Life Cycles of Landfalling Atmospheric Rivers Over the U.S. West Coast. *Journal of Geophysical Research: Atmospheres, 124*(22), 11897-11909. doi:10.1029/2019jd031218

Zhou, Y., Kim, H., & Guan, B. (2018). Life Cycle of Atmospheric Rivers: Identification and Climatological Characteristics. *Journal of Geophysical Research-Atmospheres*, *123*(22), 12715-12725. doi:10.1029/2018jd029180

Geophysical Research Letters

Supporting Information for

Atmospheric River Life Cycle Responses to the Madden Julian Oscillation

Yang Zhou[1*], Hyemi Kim[2], and Duane E. Waliser[3]

[1]Lawrence Berkeley National Laboratory, Berkeley, CA, 94720

[2]Stony Brook University, Stony Brook, NY, 11794

[3]Jet Propulsion Laboratory, California Institute of Technology, Pasadena, CA, 91109

Contents of this file

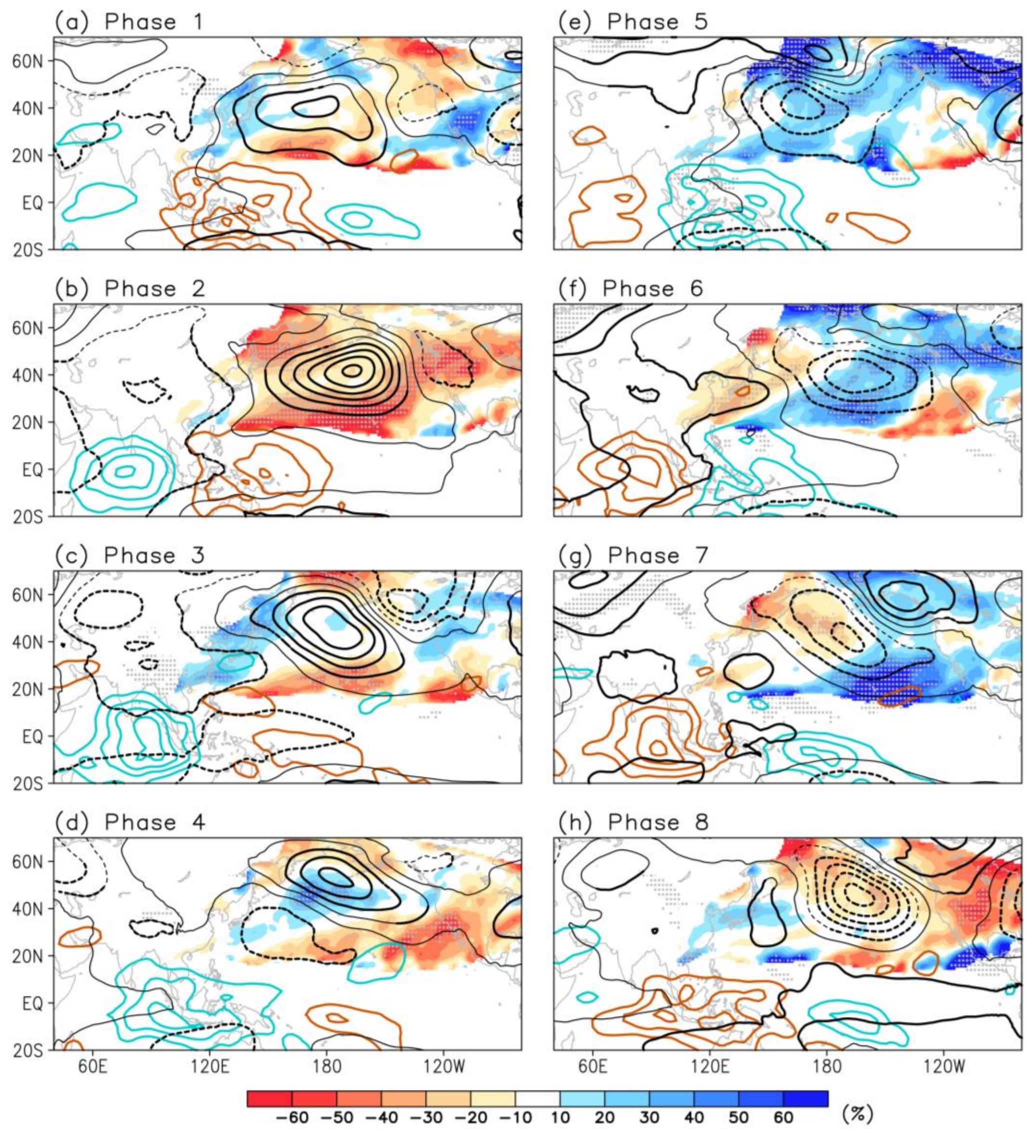

S1. Composites of percentage changes in lifecycle frequency (shading), Z850 anomaly (solid/dash contours represent positive/negative values, 5m interval), and OLR anomaly (orange/blue contours represent positive/negative values, 5 W/m^2 interval, zero line is omitted) for **a-h** MJO phase 1-8. Z850 anomaly is 10-day averaged starting from AR origins. The OLR anomaly is concurrent with AR origins. The large (small) grey dots mark AR frequency anomalies that pass the 95% (90%) confidence level of one-sample t-test. Black contours represent values that exceed the 95% confidence level of one-sample t-test.

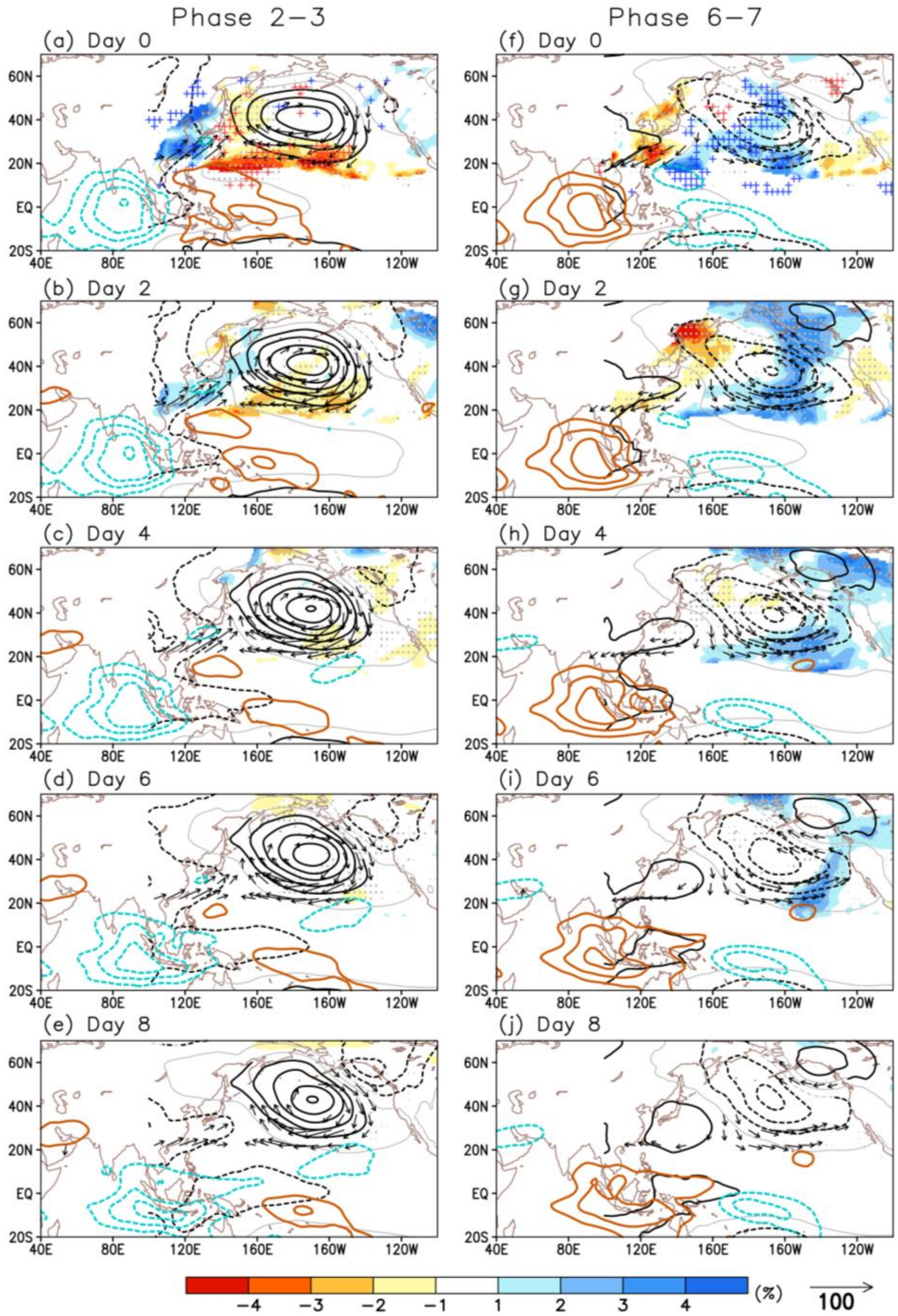

S2. Every-two-day lag composites starting from AR origins in percentage changes of lifecycle frequency (shading), Z850 anomaly (solid/dash contours represent positive/negative values, 5m interval), IVT anomaly (only showing values to the north of 10°N and over 15 kg m^{-1} s^{-1}), and OLR anomaly (orange/blue contours represent positive/negative values, 5 W/m^{2} interval, zero line is omitted) for MJO phases **a-e** 2-3 and **f-j** 6-7. Z850 and OLR anomalies are 20-100-day filtered. The large (small) grey dots mark AR frequency anomalies that pass the 95% (90%) confidence level of one-sample t-test. Black contours and shown vectors represent values that exceed the 95% confidence level of one-sample t-test. The plus sign in **a** and **f** shows anomalous origin frequency which is the same as Figure **3a-b**.

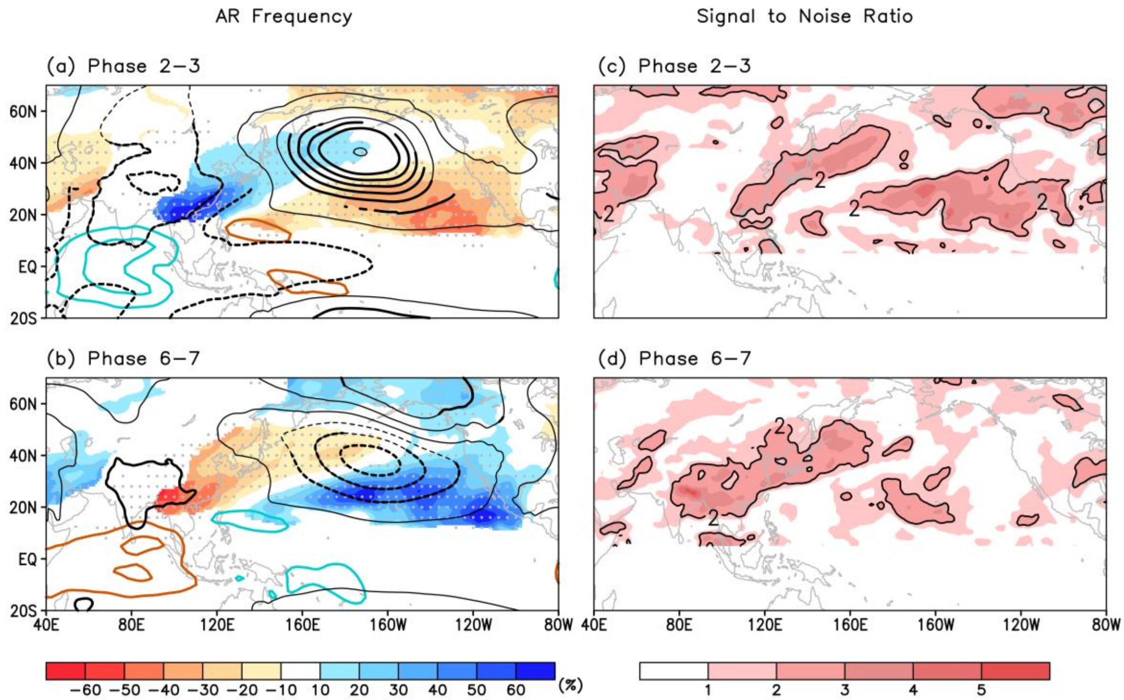

S3. a-b Composites of percentage changes in lifecycle frequency (shading), Z850 anomaly (solid/dash contours represent positive/negative values, 5m interval), and OLR anomaly (orange/blue contours represent positive/negative values, 5 W/m^2 interval, zero line is omitted) for MJO phases **a** 2-3 and **b** 6-7 using ECMWF-Hist simulations. Z850 anomaly is 10-day averaged starting from AR origins. The OLR anomaly is concurrent with AR origins. The grey dots and black contours represent values that pass the 95% confidence level of one-sample t-test. **c-d** Signal-to-noise ratio calculated by dividing **a-b** with one standard deviation of anomalous lifecycle frequency among 10 ensembles.